Photochemical & Photobiological Sciences
https://doi.org/10.1007/s43630-021-00086-y

ORIGINAL PAPERS

Revisiting the $BaBiO_3$ semiconductor photocatalyst: synthesis, characterization, electronic structure, and photocatalytic activity

Dmitry S. Shtarev[1] · Anna V. Shtareva[1] · Ruslan Kevorkyants[2] · Maxim S. Molokeev[3,4,5] · Nick Serpone[6]

Received: 31 May 2021 / Accepted: 2 August 2021

Abstract
This article revisits the properties of $BaBiO_3$ examined extensively in the last two decades because of its electronic properties as a superconductor and as a semiconductor photocatalyst. Solid-state syntheses of this bismuthate have often involved $BaCO_3$ as the barium source, which may lead to the formation of $BaBiO_3/BaCO_3$ heterostructures that could have an impact on the electronic properties and, more importantly, on the photocatalytic activity of this bismuthate. Accordingly, we synthesized $BaBiO_3$ by a solid-state route to avoid the use of a carbonate; it was characterized by XRD, SEM, and EDX, while elemental mapping characterized the composition and the morphology of the crystalline $BaBiO_3$ and its thin films with respect to structure, optoelectronic, and photocatalytic properties. XPS, periodic DFT calculations, and electrochemical impedance spectroscopy ascertained the electronic and electrical properties, while Raman and DRS spectroscopies assessed the relevant optical properties. The photocatalytic activity was determined via the degradation of phenol in aqueous media. Although some results accorded with earlier studies, the newer electronic structural data on this bismuthate, together with the photocatalytic experiments carried out in the presence of selective radical trapping agents, led to elucidating some of the mechanistic details of the photocatalytic processes that previous views of the $BaBiO_3$ band structure failed to address or clarify. Analytical refinement of the XRD data inferred the as-synthesized $BaBiO_3$ adopted the $\boldsymbol{C}_{2/m}$ symmetry rather than the $\boldsymbol{I}_{2/m}$ structure reported earlier, while Tauc plots from DRS spectra yielded a bandgap of 2.05 eV versus the range of 1.1–2.25 eV reported by others; the corresponding flatband potentials were 1.61 eV (E_{VB}) and − 0.44 eV (E_{CB}). The photocatalytic activity of $BaBiO_3$ was somewhat greater than that of the well-known Evonik P25 TiO_2 photocatalyst under comparable experimental conditions.

Graphic abstract

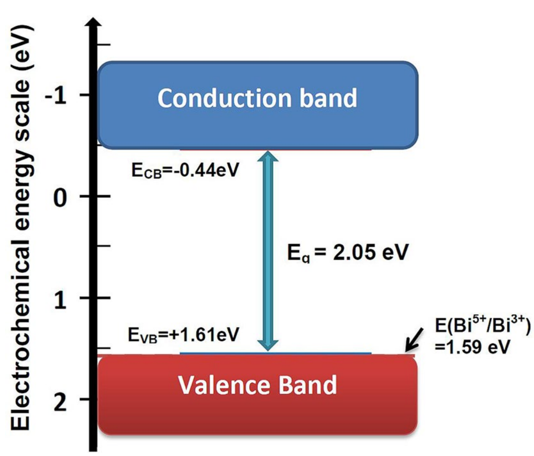

Keywords Barium bismuthate · Visible-light-active photocatalyst · Photocatalytic activity · Bandgaps · Flatband potentials

Extended author information available on the last page of the article

Published online: 17 August 2021

1 Introduction

The past two decades have witnessed a significant renaissance of the bismuthate $BaBiO_3$ from both a technological and scientific viewpoint [1–11], especially as a superconductor [1, 3, 5–7] because of its electronic properties, and as a promising photocatalyst toward the degradation of organic pollutants [2], water splitting [9, 10], CO_2 reduction [4], and as a prospective photovoltaic material [11]. The unique properties of $BaBiO_3$ are largely the result of the occurrence of both Bi^{3+} and Bi^{5+} oxidation states that have tended to complicate studies of this bismuthate. For instance, Namatame et al. [1] found the peak-to-peak splitting of the Bi_{6s} band to be large, while the minimum gap was much smaller, consistent with the large direct optical gap of ~2 eV and a smaller indirect transport gap of ~0.5 eV. Their comparison of the photoemission, optical absorption, and transport data on $BaBiO_3$ suggested the existence of polaron energy levels within the bandgap of $BaBiO_3$ that accommodate thermally excited charge carriers. Kumar and coworkers [5] synthesized this bismuthate from Bi_2O_3 and $BaCO_3$ via a two-step solid-phase heating method that, when sintered in oxygen, yielded a single-phase $BaBiO_3$ with monoclinic $\boldsymbol{I}_{2/\mathrm{mm}}$ symmetry from high-resolution XRD, while XPS confirmed the presence of two valence states of bismuth: Bi^{3+} and Bi^{5+}. Optical spectroscopy revealed a direct bandgap of ~2.2 eV and a possible indirect bandgap of ~0.9 eV, which when combined with the activation energy for conduction of 0.25 eV (*ac* impedance spectroscopy) led Kumar et al. [5] to infer a polaron-mediated conduction mechanism to prevail in $BaBiO_3$. Importantly, the optical absorption spectra given by these authors revealed yet another linear section in the Tauc plot that yields an optical bandgap of 1.67 eV (see Fig. S1 in Supplemental Information). For their part, using a two-step heating solid-state protocol, Chouhan et al. [11] prepared $BaBiO_3$ from Bi_2O_3 and $BaCO_3$ for photovoltaic applications. Their analysis of the optical transition spectra of thin films of $BaBiO_3$ featured both a direct ($E_g = 2.25$ eV) and an indirect ($E_g = 2.02$ eV) bandgap, while UPS revealed a flatband potential E_{VB} of 1.6 eV [11].

The photocatalytic properties of $BaBiO_3$ prepared from $Ba(NO_3)_2$ and $Bi(NO_3)_3{\cdot}5H_2O$ in aqueous media were first reported by Tang et al. [2] for the mineralization of acetaldehyde and methylene blue. A Tauc plot from diffuse reflectance spectra yielded a direct bandgap E_{bg} of 2.05 eV; the flatband potentials E_{VB} and E_{CB} estimated theoretically by the Butler-Ginley method gave 1.87 eV and −0.18 eV, respectively (see also Fig. S2). The authors attributed the photocatalytic activity of the $BaBiO_3$ particulates to the formation of H_2O_2 on the particle surface; the reduction half-reaction was left silent. Similarly, Ge et al. [9] prepared $BaBiO_3$ from barium and bismuth acetates dissolved in a mixture of acetic acid, 2-methoxyethanol, and acetylacetone with their goal of applying the resulting bismuthate system in the photocatalytic water splitting process. Optical transmission spectra of $BaBiO_3$ thin films yielded $E_{bg} = 1.41$ eV for direct optical transitions [9], a bandgap that differed significantly from those reported by others. The Mott–Shottky technique gave a flatband band potential E_{CB} of ca. −0.79 eV, approximately 0.5 eV greater than values determined elsewhere [2]. By contrast, Khraisheh et al. [4] examined the photocatalytic reduction of CO_2 to methane and CO under visible light in the presence of $BaBiO_3$ prepared using a high-temperature solid-phase synthesis (1100 °C for 4−5 h) using Bi_2O_3 and $BaCO_3$ as precursors; absorption spectroscopy revealed the absorption band edge to be located at 2.04 eV (= E_{bg}).

A compilation of the band structures of $BaBiO_3$ based on earlier analyses [1, 2, 9, 11] is illustrated in Fig. 1, which shows some of the disparities in regard to both bandgaps and VB/CB flatband potentials. Although the figure shows

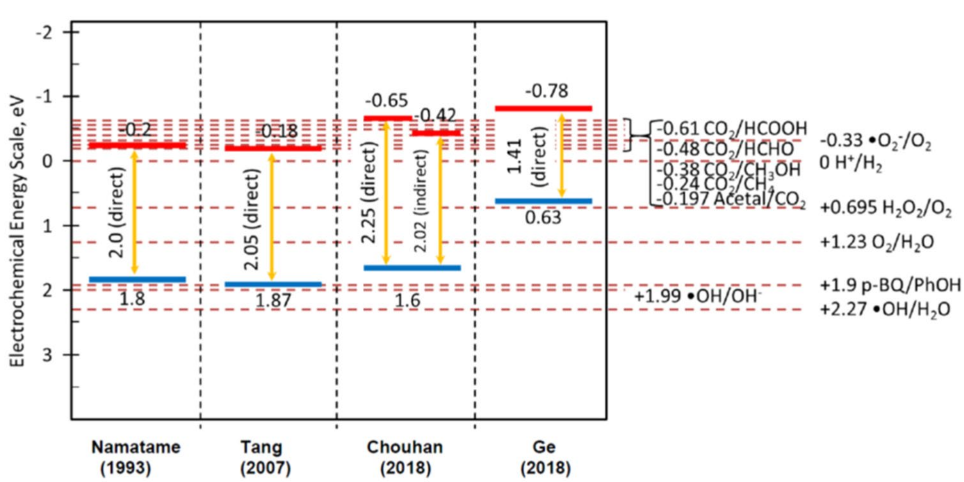

Fig. 1 Band structures of $BaBiO_3$ derived from literature analyses [1, 2, 9, 11]. The dashed lines denote various half-reactions and their corresponding redox potentials

only four examples of direct/indirect bandgaps for this bismuthate, other experimental determinations of the bandgap energy have revealed far greater disparities. For instance, Uchida et al. [12] found a direct E_{bg} of 2.0 eV for $BaBiO_3$, while others described indirect bandgaps E_{bg} of 0.2 eV [13], 0.5 eV [14], 0.8 eV [15], 1.1 eV [16], and 1.94–2.02 eV depending on temperature and preparative mode [10]. Theoretical computations of direct and indirect bandgap energies fare no better, as they are strongly dependent on the assumptions and DFT approaches taken. For instance, computed direct bandgaps vary wildly from 1.1 to 3.00 eV, whereas the indirect bandgap energies of this bismuthate range from 0.0 to 1.63 eV [17]. Also listed in Fig. 1 are some relevant redox potentials for the reduction of CO_2 (and others) to such reduced products as formaldehyde, methanol and methane. Clearly, information on the electronic structure of $BaBiO_3$ remains rather partial and controversial.

An important issue addressed in this study is the very nature of the $BaBiO_3$ obtained from various synthetic routes. Most researchers [4, 5, 11] used either $BaCO_3$ or some carbon-containing precursor to synthesize $BaBiO_3$ for which the presence of carbonate species will affect the photocatalytic activity as recently demonstrated by us [18, 19]; for example, even trace amounts of $SrCO_3$ enhanced the photocatalytic activity of strontium bismuthates. Another point addressed is the application of the Butler-Ginley method to determine the flatband potentials E_{VB} and E_{CB} as the method fails to produce accurate flatband potentials as demonstrated from a comparison of experimental and theoretical data [20, 21]. More importantly, within the context of the present study, earlier studies devoted to $BaBiO_3$ failed to address adequately the mechanistic details of the photocatalytic activity of this important bismuthate.

Accordingly, the principal objectives in revisiting the characteristics of barium bismuthate in the present study aimed at (i) a synthesis of $BaBiO_3$ that is carbonate-free, (ii) a detailed characterization of the bismuthate's band structure; and (iii) at accessing some of the mechanistic stages of the photocatalytic activity using phenol as the model substrate and various selected radical scavengers.

2 Experimental techniques and methods

2.1 Materials and synthesis

All chemical reagents for the solid-state synthesis of $BaBiO_3$ were of analytical grade (> 99.5% purity; ACROS Chemicals) and used without further purification. Unless noted otherwise, most experiments were performed using powdered $BaBiO_3$ samples prepared by a two-step heating solid-phase method using Bi_2O_3 and $Ba(NO_3)_2$ as precursors. Thus, a stoichiometric mixture of the latter two was prepared and thoroughly ground, followed by annealing at 650 °C for 10 h (first stage) that led to the complete degradation of $Ba(NO_3)_2$ to barium and gaseous nitrogen oxides. In the second stage, the resulting mixture was ground and pressed again, a process repeated every 12 h during annealing at 730 °C over a period of 72 h.

Typically, studies of the optical properties of $BaBiO_3$ were conducted with thin films prepared by dissolving powdered $BaBiO_3$ in boiling glacial acetic acid, followed by placing the solution onto a quartz substrate using the dip-coating technique, after which it was annealed in a preheated muffle furnace for 72 h at 730 °C.

2.2 Characterization of the as-prepared $BaBiO_3$

Powder diffraction data of $BaBiO_3$ for the Rietveld refinement analysis by the TOPAS 4.2 system [22] were collected at room temperature on a Bruker D8 ADVANCE powder diffractometer (Cu-Kα radiation) equipped with a linear VANTEC detector; the step size of 2θ was 0.016 degrees; counting time was 1.5 s/step. The morphology of $BaBiO_3$ was investigated by Scanning Electron Microscopy (SEM, TESCAN; accelerating voltage, 20 kV), while the elemental composition was established by Energy Dispersive X-ray Spectroscopy (EDX; model X-MaxN; Oxford Instruments). As well, the elemental composition of the surface of pure $BaBiO_3$, together with the valence band potential were determined by X-ray Photoelectron Spectroscopy (XPS) using the Thermo Fisher Scientific Escalab 250Xi spectrometer (Al Kα radiation, 1486.6 eV; spectral resolution, 0.5 eV); the C_{1s} carbon line (C−C bond) was the reference at the binding energy of 284.8 eV [23].

The specific surface area of the as-synthesized barium bismuthate particles, pretreated at 350 °C for 6 h, was obtained by the BET method using the Quadrasorb SI surface area analyzer (Quantachrome Instruments) and the curves of the physical adsorption–desorption of krypton Kr; the corresponding sizes of $BaBiO_3$ particles were measured using the Nanotrac Ultra analyzer (Anton Paar GmbH).

Raman spectra of pure $BaBiO_3$ were recorded at ambient temperature in the 80–1500 cm^{-1} spectral region using the Bruker SENTERRA Raman spectrometer (resolution, 2 cm^{-1}; excitation laser wavelength, 785 nm; laser beam power, 1 mW). Other optical properties of $BaBiO_3$ were assessed using thin films deposited on a quartz substrate. Transmission spectra were recorded in the spectral range 190–800 nm under ambient conditions using a UV-1800 UV/vis spectrophotometer. The film's width was controlled by means of optical microscopy using a Zeiss–Axio Imager. A 2 m optical microscope (Carl Zeiss Microscopy Deutschland GmbH, Germany).

The electrophysical properties of as-synthesized $BaBiO_3$ samples were ascertained by electrochemical impedance spectroscopy (EIS). The NOVOCONTROL BDS dielectric spectrometer (Novocontrol Technologies GmbH & Co. KG, Germany) provided precision measurements of the complex conductivity over a wide frequency range from 0.01 to 40 MHz and temperatures from −150 to 275 °C. The powdered samples were pressed into self-supported pellets (diameter 8.9 mm; thickness 0.62 mm).

2.3 Photocatalytic activity

The oxidative degradation of phenol in aqueous media, carried out under otherwise identical conditions used earlier for strontium bismuthates [24], was used to assess the photocatalytic activity of $BaBiO_3$ using a batch-type reactor with a lateral quartz window. The aqueous suspension of $BaBiO_3$ (loading, 1.0 g L^{-1}; pH 7.0; volume, 300 mL) was pretreated in an ultrasonic processor for 10 min, followed by the addition of phenol (purity, 99.5%; Aldrich) for a total concentration of 100 ppm (100 mg L^{-1} or 1.06 mmol L^{-1}). The suspension was subsequently stirred with a magnetic stirrer for 1 h in the dark to achieve adsorption–desorption equilibrium, after which it was irradiated with a 150-W xenon lamp (OSRAM) at wavelengths above 300 nm (cutoff filter; incident light irradiance, 7 mW cm^{-2}). Aliquots were collected at 30-min intervals, filtered through a 0.2 μm Minisart filter to remove solid particles prior to the HPLC analysis of the time-dependent phenol concentration (1260 Infinity liquid chromatograph; UV–Vis detector; Agilent Technologies C18 column); the mobile phase was a 50/50 *v*/*v* mixture of methanol/water; the detection wavelength was 210 nm. For comparison, the photocatalytic activity of Evonik's P25 TiO_2 toward the degradation of phenol was also determined under otherwise similar conditions as for the $BaBiO_3$ samples.

The photocatalytic activity of the samples was estimated from the rates of the photodegradation of phenol using $C(t) = C_0 - kt$, where C_0 is the initial phenol concentration, t is the irradiation time, and k is the zero-order rate constant.

To unravel the mechanistic details of the photocatalytic degradation of phenol, reactions were also carried out in the presence of selective radical scavengers that interact either with the photogenerated electrons (e^-) or with holes (h^+) subsequent to absorption of light energy equal to or greater than the bismuthate's bandgap. These charge carriers lead to the formation of reactive oxygen species (ROS) on the surface of $BaBiO_3$ particulates: hydroxyl radicals $\{OH^- (H_2O) + h^+ \rightarrow \cdot OH\ (+H^+)\}$ and superoxide radical anions ($O_2 + e^- \rightarrow O_2^{-\cdot}$), together with hydroperoxyl radicals $\cdot O_2H$ [25]. The selected radical scavengers interact with these species and thus prevent them from participating in the photo-oxidative degradation of phenol. For instance, isopropyl alcohol (IPA; purity > 99.9%; Panreac) scavenges ·OH radicals, while *p*-benzoquinone (*p*-BQ, purity > 98%, Sigma-Aldrich) traps $O_2^{-\cdot}$ radical anions, and ammonium oxalate (AO) competes effectively for the photoholes h^+. Dimethyl sulfoxide (DMSO) or suitable metal cations (e.g., Ag^+) also compete for the photoelectrons whenever $BaBiO_3$ particles are decorated with metal ions. However, the latter was not used in the present study, as they would have altered the nature of the initial photocatalyst and thus its subsequent photocatalytic activity.

In a typical run involving the presence of scavengers, a sample of 50 mg of $BaBiO_3$ was added to 50 mL of an aqueous phenol solution followed by the addition of 0.20 mmol L^{-1} of the selected radical scavenger [26]. Experiments were run in four photocatalytic reactors, three of which contained one of the radical scavengers (i.e., IPA or *p*-BQ or AO), while the fourth was used for comparison purposes (control). In all cases, the experimental conditions were otherwise identical as for the determination of the photocatalytic activity of $BaBiO_3$. For instance, the suspensions were exposed (but covered) to the lamps' heat for no less than 60 min to achieve adsorption–desorption equilibrium and to test for any possible thermal degradation. Thereafter, the suspension was irradiated for 8.5 h, subsequent to which appropriate aliquots were taken from all four reactors, filtered and their phenol content analyzed by liquid chromatography. The measure of the photocatalytic activity (A in % units)) in the presence of selected radical scavengers was estimated from Eq. (1).

$$A = \frac{C_o - C_{8.5}}{C_o} \times 100, \tag{1}$$

where C_o and $C_{8.5}$ are the initial ($t = 0$) and final (8.5 h) phenol concentrations, respectively.

2.4 Computational details

The electronic structure of $BaBiO_3$ was determined by a periodic DFT approach using the Local Density Approximation [27] and the Generalized Gradient Approximation with Perdew-Burke-Ernzerhof (PBE) density functionals [28, 29] as implemented in the ABINIT 6.8.3 program [30]. The basis sets employed the form of norm-conserving Troullier-Martins (TM) [31] and relativistic Hartwigsen-Goedecker-Hutter [32] pseudopotentials with the kinetic energy cutoff of 30 and 50 Hartree, respectively. Spin–orbit coupling (SOC) interactions were taken into account through a scalar-relativistic approach. The Brillouin Zone (BZ) was sampled over the automatically generated Γ-point-centered 8 × 8 × 8 Monkhorst–Pack grid of k-points [33]. The electronic band structures were thus computed at 181 k-points along the Γ-A-C-D-D1-E-X–Y-Y1-Z high symmetry path of the monoclinic $C_{2/m}$ BZ. We applied the energy convergence criterion of 10^{-8} Hartree. The resulting band structures and

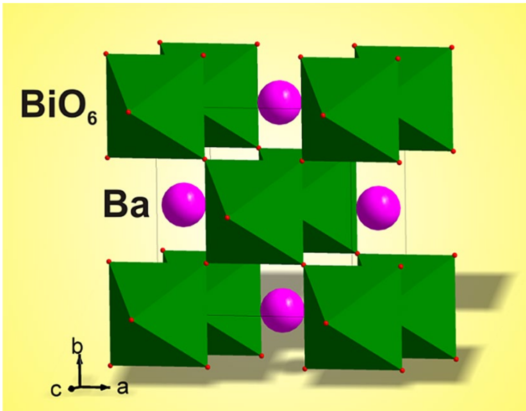

Fig. 2 Cartoon illustrating the $\boldsymbol{C}_{2/\mathrm{m}}$ crystal structure of the as-prepared $BaBiO_3$ by the solid-state synthesis

Table 1 Principal parameters of the processing and refinement of $BaBiO_3$

Compound	$BaBiO_3$
Space group	$\boldsymbol{C}_{2/m}$
a, Å	6.1869 (1)
b, Å	6.1392 (2)
c, Å	4.3349 (1)
β, °	89.824 (1)
V, Å^3	164.648 (7)
Z	2
2θ-interval, °	15−140
R_{wp}, %	9.54
R_p, %	7.39
R_{exp}, %	5.94
χ^2	1.61
R_B, %	3.26

density of states were plotted using the Gnuplot 5.2 software package [34].

3 Results

3.1 Rietveld refinement of the $BaBiO_3$ crystal structure

The earlier refinement by Efremov and coworkers [35] of the crystal structure of $BaBiO_3$ assigned it to the $\boldsymbol{I}_{2/\mathrm{m}}$ space group with cell parameters: $a=6.1736$ Å, $b=6.1237$ Å, $c=8.6507$ Å, $\beta=90.29°$ and $V=327.038$ Å^3. Initially, we used this assignment to interpret our XRD data of the as-prepared $BaBiO_3$. However, we failed to get a good profile fitting and achieved an R-factor of only 12.38%. Consequently, we indexed our experimental XRD pattern using the Topas 4.2 program [22] that resulted in assigning the structure of $BaBiO_3$ to the $\boldsymbol{C}_{2/\mathrm{m}}$ space group with cell parameters: $a=6.183$ Å, $b=6.140$ Å, $c=4.334$ Å, $\beta=89.82°$, $V=164.53$ Å^3 that gave a figure of merit of 20.3%. The two cells could not be transformed into each other because of a large difference in cell volumes. The smaller cell with $\boldsymbol{C}_{2/\mathrm{m}}$ symmetry was advantageous as the number of refinement parameters was significantly smaller. We utilized the parent cubic $\boldsymbol{P}_{\mathrm{m3m}}$ phase of $BaBiO_3$ and distorted it down to the $\boldsymbol{C}_{2/\mathrm{m}}$ symmetry using the ISODISTORT internet tool [36] to determine the atomic coordinates. As a result, all ions were located in special positions (see Fig. 2); their coordinates needed no further refinement.

The refinement was stable and gave low R-factors (Table 1, Fig. 3); for example, the R-factor dropped to 9.54% in comparison to that of the $\boldsymbol{I}_{2/\mathrm{m}}$ model. Crystal structure tests with the CheckCif internet tool [37] revealed the following missing symmetry elements '3', '4', 'm' and suggested the $\boldsymbol{P}_{\mathrm{m3m}}$ space group rather than

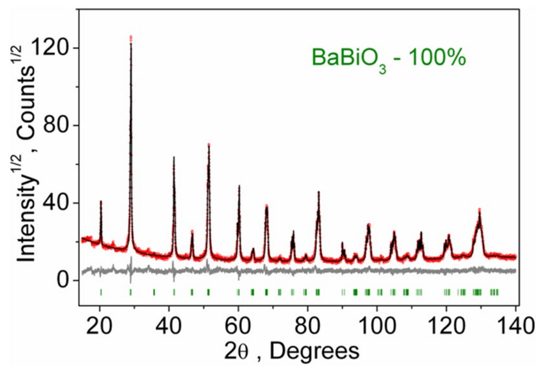

Fig. 3 Difference Rietveld plots of the $C_{2/\mathrm{m}}$ (red) versus the P_{m3m} structure (black) of $BaBiO_3$

Table 2 $BaBiO_3$ fractional atomic coordinates and isotropic displacement parameters, Å^2

	X	Y	Z	B_{iso}
Ba	0	1/2	½	0.70 (4)
Bi	0	0	0	0.50 (4)
O_1	¼	1/4	0	3.0 (2)
O_2	0	0	½	3.0 (2)

Table 3 Main bond lengths (Å) of $BaBiO_3$

Ba—O_1	3.0700 (1)	Ba—O_2^{ii}	3.0935 (1)
Ba—O_1^{i}	3.0767 (1)	Bi—O_1	2.1790 (1)
Ba—O_2	3.0696 (1)	Bi—O_2	2.1674 (1)

Symmetry codes: (i) x, y, $z+1$; (ii) $-x+1/2$, $-y+1/2$, $-z+1$

$\boldsymbol{C}_{2/\mathrm{m}}$. However, the main peak splitting in the powder pattern (Fig. 3) showed that a cubic phase was not possible and such peak splitting could only be fitted by a monoclinic unit cell. Therefore, the proposed $\boldsymbol{C}_{2/\mathrm{m}}$ unit cell was considered more appropriate as it fitted well with the XRD pattern.

Tables 2 and 3 report the corresponding atomic coordinates and selected bond lengths, respectively. For further details, see Fachinformationszentrum Karlsruhe [38]; deposition number CSD-2055389.

3.2 Raman spectroscopy

Figure 4 displays both the original Raman spectrum and its baseline-corrected spectrum of the as-synthesized $BaBiO_3$, which reveals a low-intensity narrow signal with a maximum at 307.4 cm^{-1} accompanied by a significantly broader signal that spans the 400−600 cm^{-1} region, which consists of three Gaussian signals at 477.0 cm^{-1}, 510.0 cm^{-1} and 562.3 cm^{-1}. The spectrum accords with those from Raman spectra of $BaBiO_3$ reported by others [9, 39].

Assignment of vibrational modes in the Raman spectrum of $BaBiO_3$ has been somewhat controversial as Ba−O modes in BaO observed by de Waal et al. [40] occur at 513, 477, and 465 cm^{-1}. Nonetheless, the intense signal at 562.3 cm^{-1} likely corresponds to the A_g breathing mode of BiO_6 octahedra, whereas the signal at 307.4 cm^{-1} is likely due to the asymmetrical breathing mode of the BiO_6 octahedra [39], although Talha and Lee [41] assigned it to a Bi–O bending mode. A detailed consideration of the broad intense Raman signal at 564 cm^{-1} reported by Ge et al. [9] and by Talha and Lee [41] also consists of a contribution from a lesser intense signal at 490−492 cm^{-1} that corresponds to a Bi−O stretching mode.

The Bi−O bond lengths (R; in Å units) are related to the Raman scattering frequency υ (cm^{-1}) through the empirical Eq. (2) [42]. Thus, the frequencies 307.4 cm^{-1} and 562.3 cm^{-1} correspond to Bi−O bond lengths of 2.27 Å and 2.03 Å, respectively, and accord rather well with the Bi−O bond lengths determined earlier using the Rietveld method: 2.1790 Å and 2.1674 Å (see Table 3).

$$\upsilon = 92760e^{-2.511R}, \quad (2)$$

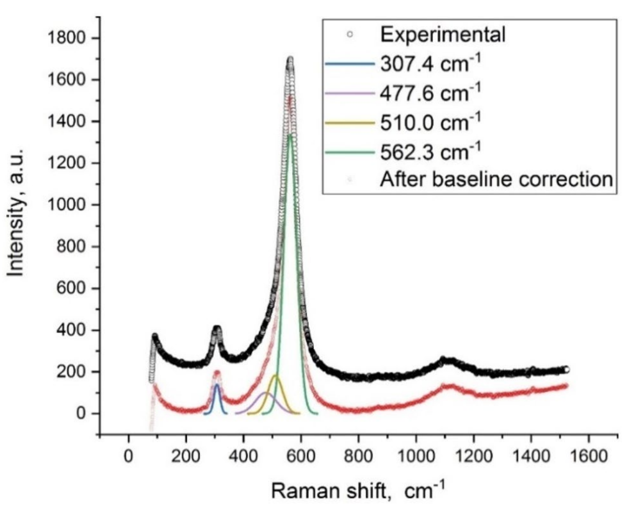

Fig. 4 Raman spectra of the as-synthesized $BaBiO_3$; the black spectrum refers to experimental data, while the red spectrum refers to experimental data after baseline correction

3.3 SEM and EDX characterization of $BaBiO_3$

Figure 5 illustrates (a) the SEM images, (b) the EDX spectra, and the elemental mapping (lower panel) of a typical as-synthesized $BaBiO_3$ particle. SEM reveals no morphological peculiarities (pores, layers and others) for the particle, while the EDX spectrum shows that the ratio Ba/Bi in the particle is very close to being stoichiometric in atom % ($Ba_{13.7}Bi_{12.6}O_{73.8}$ or $Ba_{1.1}BiO_{5.9}$). The elemental mappings reveal homogeneity among the particles.

3.4 Specific surface area and particle size distribution

The specific surface area of the as-synthesized $BaBiO_3$ particulates was estimated by the BET method (0.472 m^2 g^{-1}) and was somewhat less than the 1.2 m^2 g^{-1} reported by Tang et al. [2] who prepared $BaBiO_3$ with a perovskite structure by a soft chemical method, yet an order of magnitude greater than 0.047 m^2 g^{-1} reported by Khraisheh et al. [4] who used a conventional solid-state reaction method. Figure 6 illustrates the histogram of the estimated size distribution of $BaBiO_3$ particles, a large number of which have sizes in the range 409−486 nm.

3.5 Characterization of $BaBiO_3$ in thin films

The optical properties of $BaBiO_3$ were examined as thin films deposited on a quartz substrate subsequent to being analyzed first by optical spectroscopy. Figure 7 illustrates the surface of one such film, which shows it to be regular and to cover the whole quartz substrate; photographs of the surface of the quartz substrate and the edge of the film are reported in Fig. S3.

Figure 8 depicts XRD diffractograms of the amorphous quartz substrate and the $BaBiO_3$ thin film. Evidently, in comparison with the reference XRD pattern of $BaBiO_3$ (PDF Card No.: 01-074-7522, inset in Fig. 8) the XRD shows the film to be composed of well-formed crystalline $BaBiO_3$ particles. Consequently, this film proved suitable for investigating the transmittance spectra of $BaBiO_3$ to assess the bandgap energy.

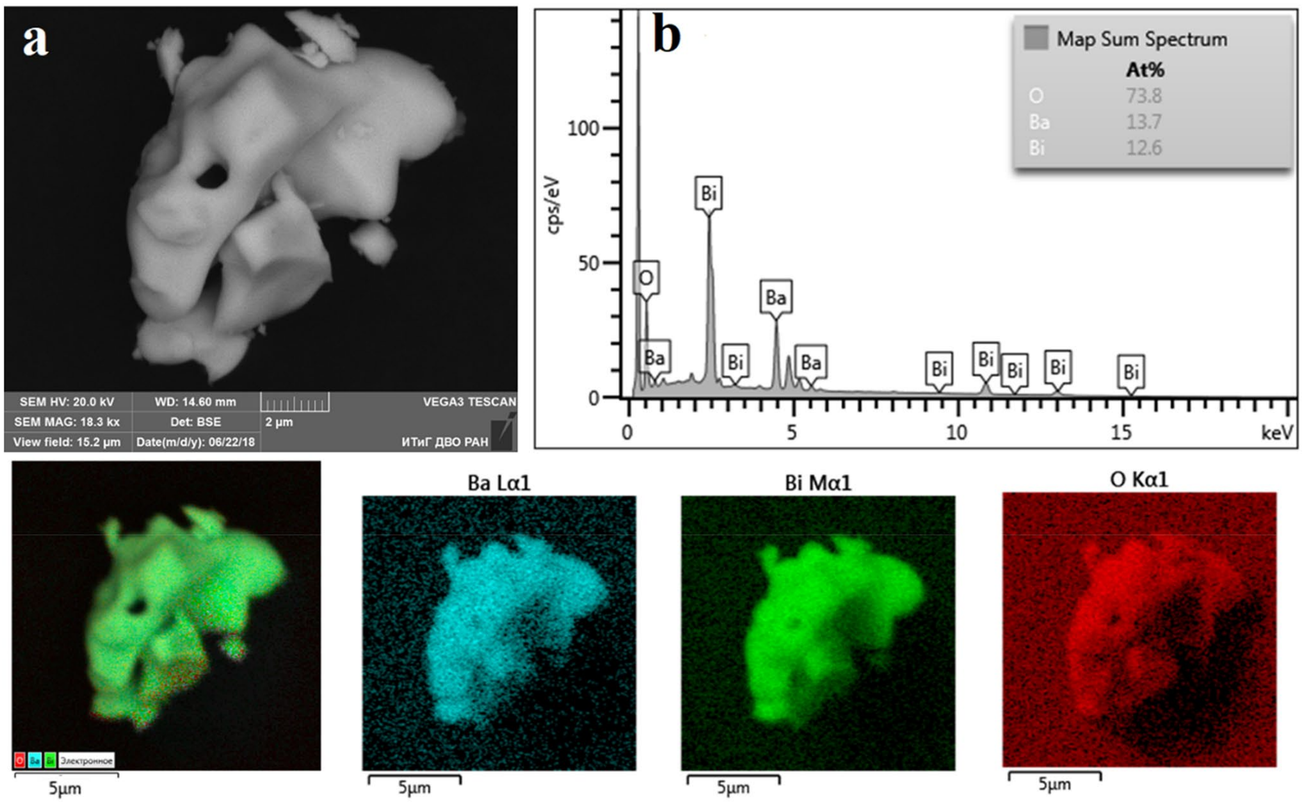

Fig. 5 Typical particle of $BaBiO_3$: **a** SEM image; **b** EDX spectrum; lower panel displays the elemental mapping

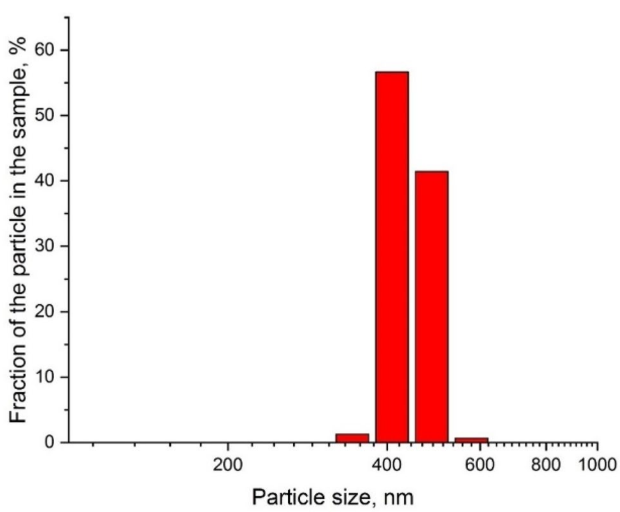

Fig. 6 Histogram displaying the size distribution of the as-synthesized $BaBiO_3$ particles

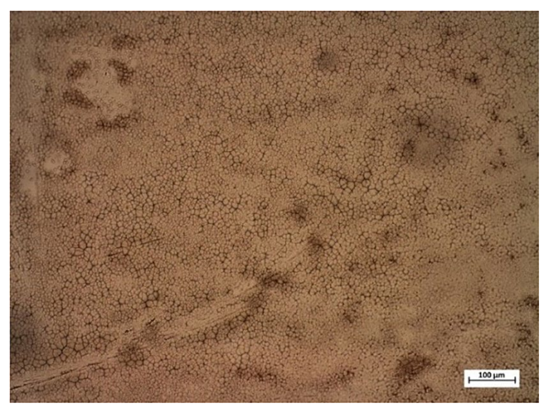

Fig. 7 Optical microscopic image of the surface of a $BaBiO_3$ thin film

3.6 Optical properties of $BaBiO_3$ in thin films

Ordinarily, an insight into the optical properties of materials implies studies of diffuse reflectance spectra and their subsequent Kubelka–Munk transformation. Unfortunately, this approach was not appropriate for studies of the $BaBiO_3$ bismuthate in powdered form. The optical absorption spectrum of powdered $BaBiO_3$, derived from the diffuse reflectance spectrum (see Fig. S4), reported as $A = (1 - R)$, showed significant absorption (0.7−0.9 in relative units) in the range from the UV to the Near IR spectral region. Consequently, it precluded the application of the Kubelka–Munk transformation and the subsequent determination of the bandgap energy through the usual Tauc plots. By contrast, the optical

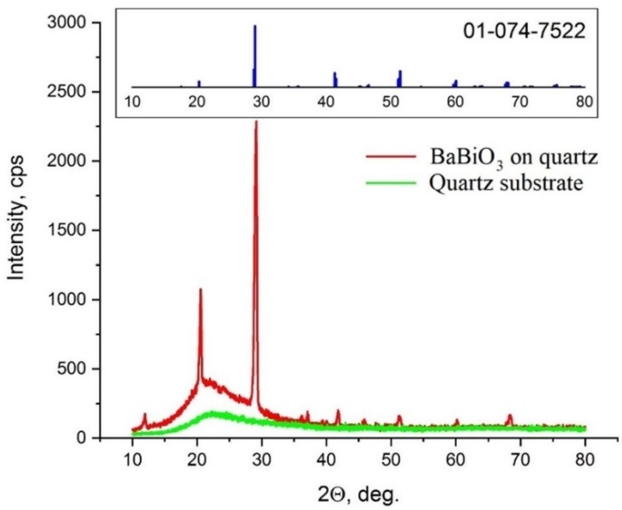

Fig. 8 XRD of the quartz substrate (green) and of a thin film of $BaBiO_3$ on quartz (red). The inset displays the reference XRD pattern of $BaBiO_3$

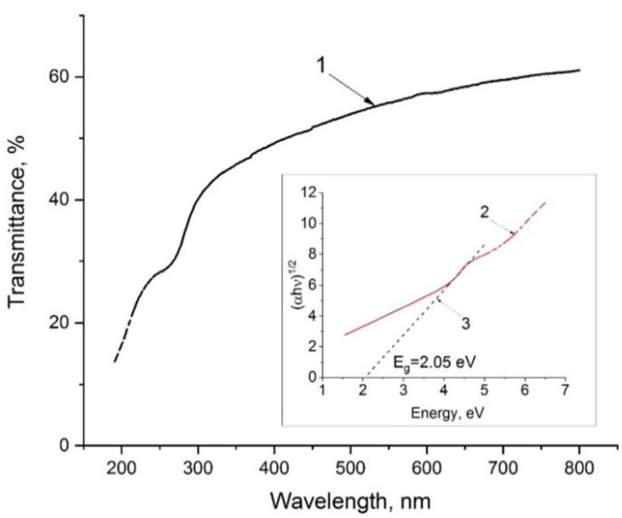

Fig. 9 Optical transmission spectrum of the $BaBiO_3$ thin film (**1**). Inset shows the Tauc plot (**2**) and its linear extrapolation (**3**) to estimate the bandgap energy

transmission spectrum of the $BaBiO_3$ thin film, illustrated in Fig. 9 (curve **1**), makes it possible to apply the Tauc method to this spectrum (inset Fig. 9), which reveals a bandgap energy E_{bg} for $BaBiO_3$ of 2.05 eV in accord with earlier reports [1, 2, 11].

3.7 XPS and band structure of $BaBiO_3$

The XPS spectral bands of the chemical elements in $BaBiO_3$ presented in Fig. 12 reveal a single Gaussian-like band for Ba (Fig. 10a) at 779.2 eV in line with the bonding energy of barium in BaO [23], while Bi presents a doublet (Fig. 10b) each of which is also a Gaussian with maxima at 163.9 eV and 158.6 eV corresponding to $Bi_{4f5/2}$ and $Bi_{4f7/2}$, respectively. All the bismuth species at the $BaBiO_3$ particle surface are present as Bi^{3+}, a point emphasized earlier [1, 11] and conforms with the observation that about half of the bismuths in the bulk of $BaBiO_3$ particles are present as Bi^{5+}. In contrast, the oxygen band in Fig. 10c is complex and could be approximated by a sum of two Gaussians with the lower energy signal at 528.6 eV corresponding to O^- species, while the higher energy line at 530.6 eV is associated with O^{2-}. The presence of O^- in alkali earth metal bismuthates noted earlier in our studies [25, 43, 44], as well as by others [45], is thus confirmed.

The energy of the top level of the valence band (E_{VB}) of $BaBiO_3$ was assessed from the low-energy band edge of the XPS spectrum of O_{2p} displayed in Fig. 11 [46], which yields an $E_{VB} = 1.61$ eV in perfect accord with the value 1.60 eV obtained by Chouhan et al. [11] (see also Fig. S2).

Consequently, the above results and studies by others infer a band structure for $BaBiO_3$ illustrated in Fig. 12, which emphasizes not only the bandgap of 2.05 eV, but more importantly the position of the flatband potential E_{VB} (= 1.61 eV). An earlier report [47] noted a strong equivalence with the redox potential of 1.59 eV for the half-reaction $Bi^{3+} \rightarrow Bi^{5+}$, in line with the notion that the bulk of $BaBiO_3$ contains about equal amounts of Bi^{3+} and Bi^{5+}. Such equivalence will have certain consequences.

It is useful to compare the experimental band structure of $BaBiO_3$ to the theoretical structure with the latter depending strongly on the approach taken. For instance, the PBE density functional predicts a metallic band structure with zero bandgap, which obviously contradicts experimental observations. Rigorous computations have uncovered the semiconducting nature of this bismuthate, which predicted the electronic bandgap to vary from 0.84 eV (HSE) to 1.63 eV (GW) [17]. Our own computations suggest that spin-orbit coupling (SOC) interactions are important factors in determining the bandgap of $BaBiO_3$. Thus, Fig. 13a displays the band structure of the bismuthate's unit cell computed using the LDA + SOC approach. It is evident that the compound features an indirect electronic transition $D1 \rightarrow E$ of 0.72 eV.

As noted above, the bulk of $BaBiO_3$ contains both Bi^{3+} and Bi^{5+} species so that computations with a single unit cell cannot account for such complexity. Consequently, we carried out LDA + SOC computations of the $BaBiO_3$ band structure with a doubled unit cell illustrated in Fig. 13b as a folded band structure. Comparison with the unfolded band structure reported in Fig. 13c suggests $BaBiO_3$ to be characterized by both direct and indirect electronic transitions of 1.69 eV ($\boldsymbol{E} \rightarrow \boldsymbol{E}$) and 1.55 eV ($\boldsymbol{E} \rightarrow \boldsymbol{E}/\boldsymbol{X}$), respectively, in good agreement with the data reported recently by Chouhan and coworkers [11]. The greater bandgap energy from the

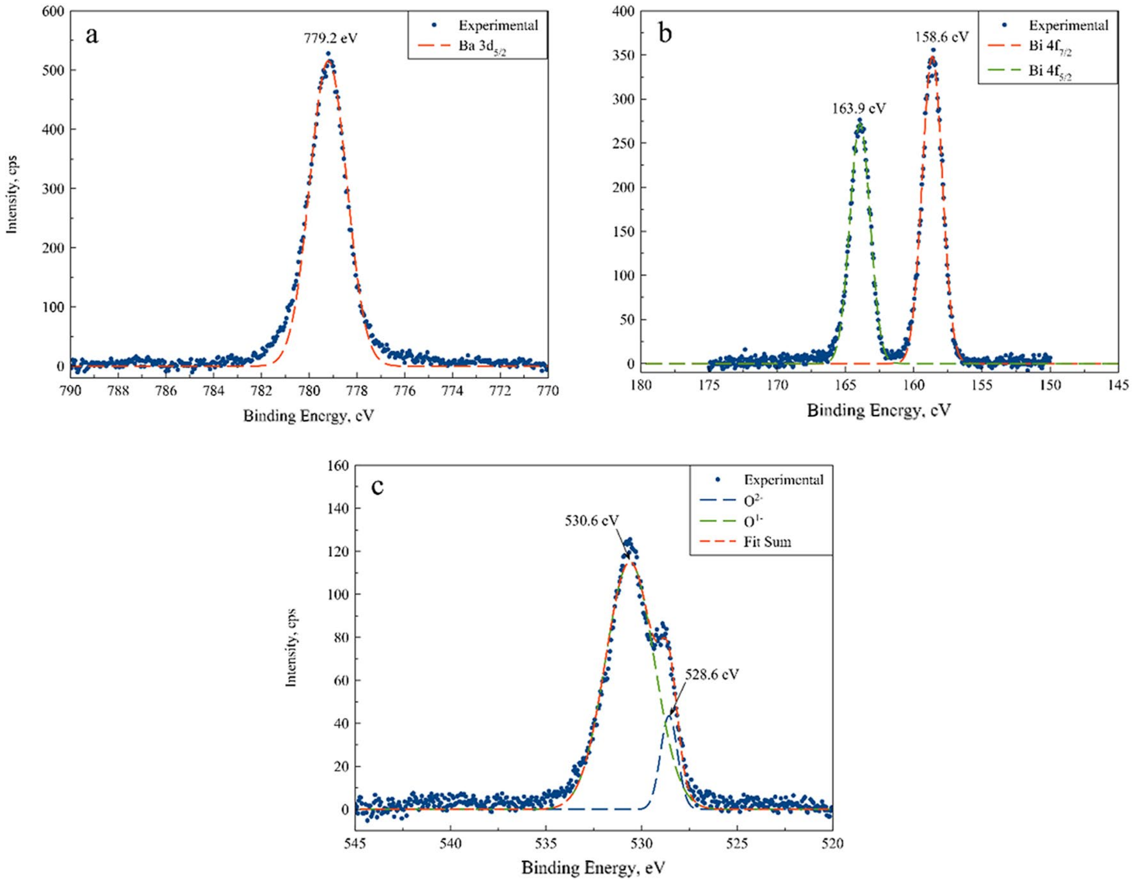

Fig. 10 XPS spectra of the chemical elements constituting $BaBiO_3$: **a** Barium; **b** Bismuth; **c** Oxygen

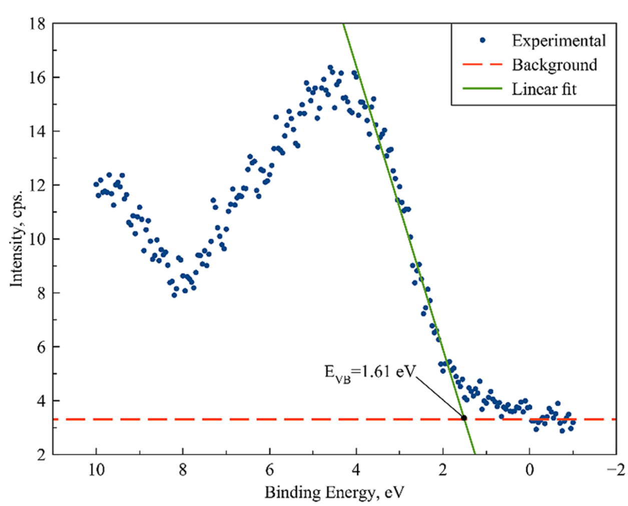

Fig. 11 XPS spectrum of $BaBiO_3$. The dashed line is a baseline, whereas the solid line is a linear extrapolation of the spectrum's low-energy band edge. The binding energy is given relative to the electrochemical scale in accordance with the methodology proposed in Ref. [44]

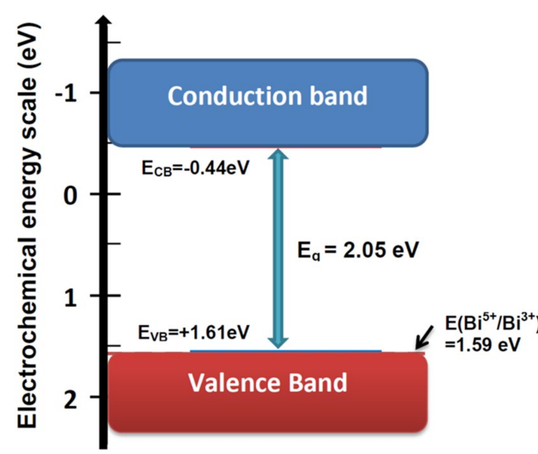

Fig. 12 Inferred band structure of $BaBiO_3$ based on an electro-chemical energy scale

experiment (2.05 eV) might possibly be caused by bandgap widening from thermal lattice expansion under the prevalent experimental conditions. Nonetheless, the bandgaps computed herein correlate well with those reported by Franchini and coworkers [17]. Results obtained from the simulation

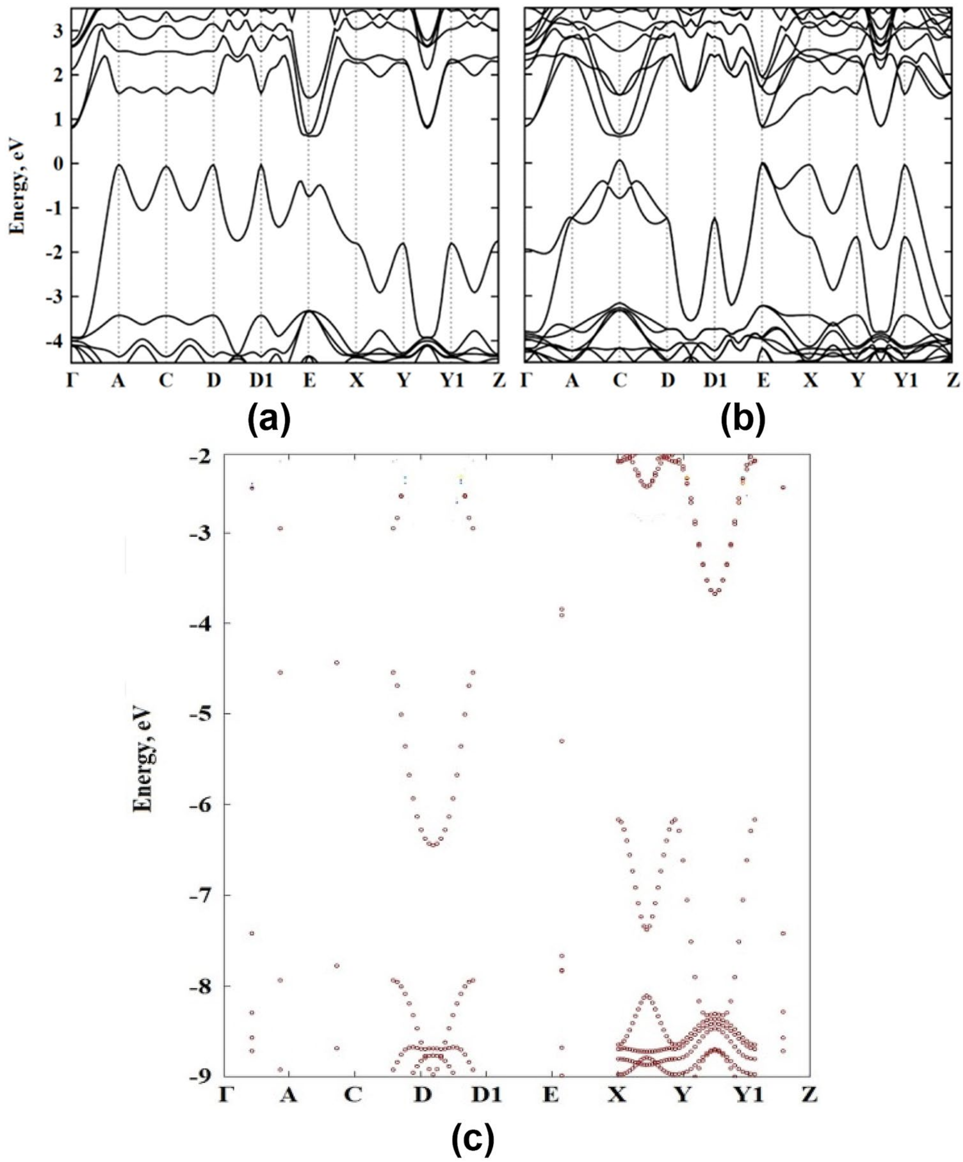

Fig. 13 LDA + SOC computed band structure of $BaBiO_3$: **a** single unit cell, **b** doubled unit cell, **c** unfolded band structure of the doubled unit cell

also explain why an indirect optical transition appeared in our study of the optical properties of thin films. To the extent that its energy is somewhat less than the energy of the direct transition explains why we failed to detect the direct optical transition experimentally.

3.8 Photocatalytic activity of $BaBiO_3$

Figure 14 reports the time course of the photocatalytic degradation of phenol in aqueous media in the presence of $BaBiO_3$, while the inset shows the zero-order degradation rates for the control experiment in the absence of $BaBiO_3$, and for comparison also reported is the degradation rate of the reaction catalyzed by Evonik's P25 TiO_2. Evidently, under otherwise comparable experimental conditions, the reaction proceeds somewhat faster in the presence of the visible-light-active $BaBiO_3$ photocatalyst than in the presence of the otherwise UV-light-active TiO_2 photocatalyst.

Experiments conducted in the presence of selective radical scavengers disclosed some of the mechanistic details of the degradation of phenol in the presence of $BaBiO_3$. The relative degradation efficiencies are displayed in Fig. 15, which shows that the usage of p-benzoquinone and ammonium oxalate lowered the rate of phenol degradation more than threefold. The active species that played a key role in this photocatalytic reaction appear to be the superoxide radical anions $O_2^{-\bullet}$ and the photoholes h^+.

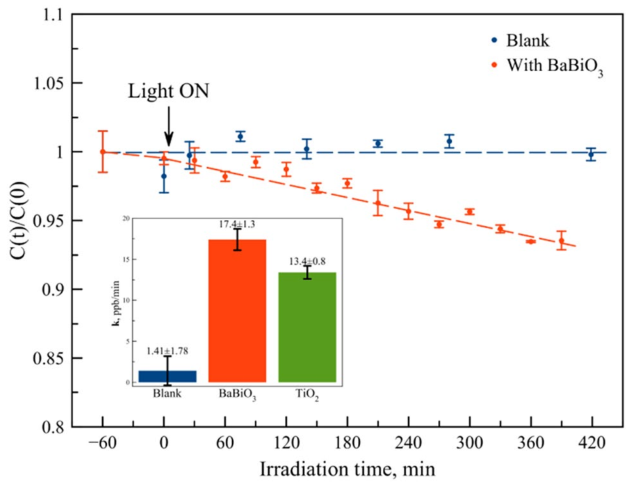

Fig. 14 Kinetics of the photocatalytic degradation of phenol with and without the presence of the $BaBiO_3$ photocatalyst. Inset reports the resulting zero-order degradation rates. For comparison, the degradation rate of phenol in the presence of Evonik's P25 TiO_2 is also reported

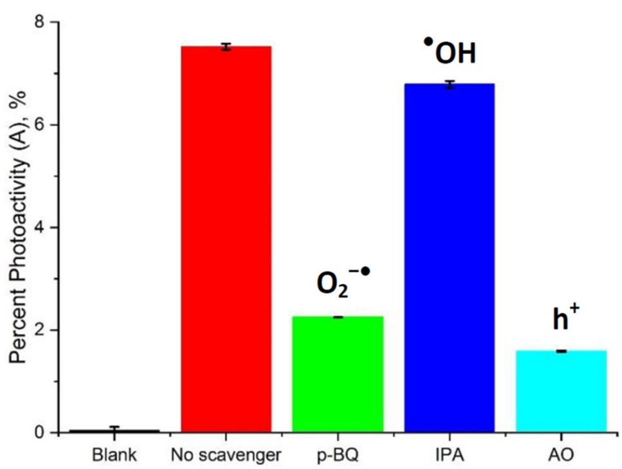

Fig. 15 Percent photocatalytic activity of $BaBiO_3$ in the photo-catalyzed degradation of phenol in the presence of various selective radical scavengers

4 Discussion and concluding remarks

We begin by addressing some of the inconsistencies arising when the experimental data on the photocatalytic activity of $BaBiO_3$ are compared to its band structure (Fig. 1). For instance, according to Tang and coworkers [2], acetaldehyde can be degraded photocatalytically in the presence of $BaBiO_3$, yet the redox potential of this reaction is − 0.197 eV [48]. However, given the E_{CB} of $BaBiO_3$ of − 0.18 V reported by these authors, the reaction is energetically unfavorable. Such a contradiction is precluded if the band structure of $BaBiO_3$ were the one inferred in the present study, which places the position of E_{CB} at − 0.44 eV, enough to allow the photocatalytic degradation of acetaldehyde to occur. Likewise, Kraisheh et al. [4] carried out the photocatalytic conversion of CO_2 to CH_4 in the presence of $BaBiO_3$, a process that requires a redox potential of − 0.24 V [49]. However, to the extent that the E_{CB} potentials reported by Namatame et al. [1] and Tang et al. [2] are − 0.20 V and − 0.18 V, respectively, such a conversion should not take place, unless of course the E_{CB} were − 0.44 eV as in the present study. For their part, Ge et al. [9] proposed the use of $BaBiO_3$ for the photocatalytic water splitting process. However, the band structure of $BaBiO_3$ reported in their study (see Fig. 1) precluded this process from occurring as the E_{VB} of 0.625 V reported by these authors is insufficient for overcoming the potential barrier of the oxidation half-reaction of oxygen formation that requires 1.23 V. The band structure of $BaBiO_3$ suggested in the present study avoids these conundrums, as the positions of both E_{VB} (1.61 V) and E_{CB} (− 0.44 V) are sufficient for the oxidation and reduction half-reactions to occur that would lead to the formation of oxygen and hydrogen, respectively.

Accordingly, $BaBiO_3$ was characterized and its band structure determined (Fig. 12) that bares close resemblance to the structure reported earlier by Chouhan and coworkers [11]. This bismuthate demonstrated a relatively higher photocatalytic activity than the well-known Evonik P25 TiO_2 toward the degradation of phenol in aqueous media. The usage of selective radical scavengers helped to clarify some details of the photocatalytic accomplishment of $BaBiO_3$ that were not addressed in previous studies. The use of radical scavengers has inferred a plausible mechanism in the photocatalytic degradation of phenol in aqueous media.

Figure 16 summarizes our current understanding of the photocatalytic mechanism of $BaBiO_3$. Upon irradiation with

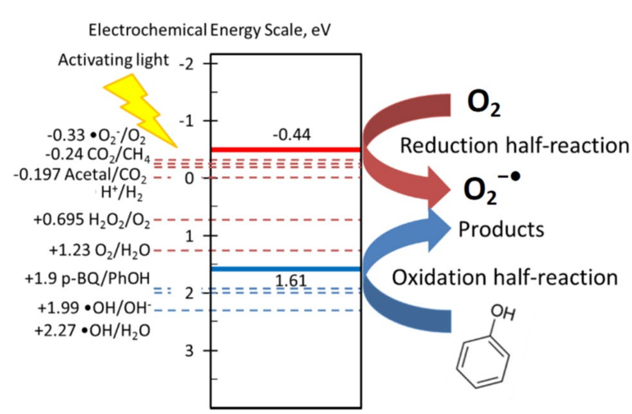

Fig. 16 Energetic scheme of the electrochemical reactions potentially photocatalyzed by $BaBiO_3$

UV/Visible light, the pair of charge carriers—photoelectrons e^- and photoholes h^+—are generated with the photoelectrons being trapped by the oxygen dissolved in the aqueous solution and adsorbed on the $BaBiO_3$ surface to yield superoxide radical anions $O_2^{-\bullet}$. The subsequent attack of phenol by this radical concludes the reduction half-reaction.

The photocatalytic tests conducted in the presence of selective radical trapping agents also infer that the photoholes h^+ played a non-insignificant role, even though the direct attack of the phenol by photoholes is precluded toward an oxidative half-reaction as the redox potential for such a process is 1.90 V [50], greater than the flatband potential E_{VB}. For the same reason, the hydroxyl radical •OH cannot participate directly in the photocatalytic process as the redox potential of its formation is greater than that of E_{VB}. Accordingly, secondary electrochemical reactions involving photoholes h^+ may be implicated. For instance, the formation of oxygen from water necessitating a redox potential of 1.23 eV, or formation of hydrogen peroxide [2] from the dissolved oxygen in the aqueous medium that requires 0.695 eV are potentially possible, in which case the hydrogen peroxide formed could directly participate in the oxidation of phenol.

Supplementary Information The online version contains supplementary material available at https://doi.org/10.1007/s43630-021-00086-y.

Acknowledgements We wish to thank the Russian Science Foundation for a Grant (Project No. 19-73-10013) in support of our study. The authors are also grateful to the staff of the following Institutes/Centers for their valuable technical assistance and in providing the needed equipment: (i) the Khabarovsk Innovation and Analytical Center of the Yu. A. Kosygin Institute of Tectonics and Geophysics FEB RAS; and (ii) the Resource Centers of the Research Park at Saint-Petersburg State University, especially the Center for Physical Methods of Surface Investigation and the Nanophotonics Center. One of us (NS) is grateful to the staff of the PhotoGreen Laboratory of the University of Pavia, Italy, for their continued hospitality.

Declarations

Conflict of interest The authors declare that they have no conflict of interest.

References

1. Namatame, H., Fujimori, A., Takagi, H., Uchida, S., de Groot, F. M. F., & Fuggle, J. C. (1993). Electronic structure and the metal-semiconductor transition in $BaPb_{1-x}Bi_xO_3$ studied by photoemission and x-ray absorption spectroscopy. *Physical Review B: Condensed Matter, 48*, 16917–16925.
2. Tang, J., Zou, Z., & Ye, J. (2007). Efficient photocatalysis on $BaBiO_3$ driven by visible light. *Journal of Physical Chemistry C, 111*, 12779–12785.
3. Yan, B., Jansen, M., & Fesler, C. (2013). A large-energy-gap oxide topological insulator based on the superconductor $BaBiO_3$. *Nature Physics, 9*, 709–711.
4. Khraisheh, M., Khazndar, A., & Al-Ghouti, M. A. (2015). Visible light-driven metal-oxide photocatalytic CO_2 conversion. *International Journal of Energy Research, 39*, 1142–1152.
5. Kumar, N., Golledge, S. L., & Cann, D. P. (2016). Synthesis and electrical properties of $BaBiO_3$ and high resistivity $BaTiO_3$–$BaBiO_3$ ceramics. *Journal of Advanced Dielectrics, 6*, 1650032.
6. Plumb, N. C., Gawryluk, D. J., Wang, Y., Ristic, Z., Park, J., Lv, B. Q., Wang, Z., Matt, C. E., Xu, N., Shang, T., Conder, K., Mesot, J., Johnston, S., Shi, M., & Radovic, M. (2016). Momentum-resolved electronic structure of the high-Tc superconductor parent compound BaBiO3. *Physical Review Letters, 117*, 037002.
7. Bhatia, A., Hautier, G., Nilgianskul, T., Miglio, A., Rignanese, G.-M., Gonze, X., & Suntivich, J. (2016). High-mobility bismuth-based transparent *p*-type oxide from high-throughput material screening. *Chemistry of Materials, 28*, 30–34.
8. Weng, B., Xiao, Z., Meng, W., Grice, C. R., Poudel, T., Deng, X., & Yan, Y. (2017). Bandgap engineering of barium bismuth niobate double perovskite for photoelectrochemical water oxidation. *Advanced Energy Materials, 7*, 1602260.
9. Ge, J., Yin, W.-J., & Yan, Y. (2018). Solution-processed Nb-substituted $BaBiO_3$ double perovskite thin films for photoelectrochemical water reduction. *Chemistry of Materials, 30*, 1017–1031.
10. Huerta-Flores, A. M., Sánchez-Martínez, D., del Rocío Hernández-Romero, M., Zarazúa-Morín, M. E., & Torres-Martínez, L. M. (2019). Visible-light-driven $BaBiO_3$ perovskite photocatalysts: Effect of physicochemical properties on the photoactivity towards water splitting and the removal of rhodamine B from aqueous systems. *Journal of Photochemistry and Photobiology A: Chemistry, 368*, 70–77.
11. Chouhan, A. S., Athresh, E., Ranjan, R., Raghavan, S., & Avasthi, S. (2018). $BaBiO_3$: a potential absorber for all-oxide photovoltaics. *Materials Letters, 210*, 218–222.
12. Uchida, S., Kitazawa, K., & Tanaka, S. (1987). Superconductivity and metal-semiconductor transition in $BaPb_{1-x}Bi_xO_3$. *Phase Transitions, 8*, 95–128.
13. Sleight, A. W., Gillson, J. L., & Bierstedt, P. E. (1975). High-temperature superconductivity in the $BaPb_{1-x}Bi_xO_3$ systems. *Solid State Communications, 17*, 27–28.
14. Takagi, H., Uchida, S., Tajima, S., Kitazawa, K., & Tanaka, S. (1986). *Proc. Intern. Conf. Physics of Semiconductors*, Stockholm, Sweden; O. Engstrom (Ed.), World Scientific Publishers, Singapore, p. 1851.
15. Kim, K. H., Jung, C. U., Noh, T. W., & Kim, S. C. (1997). Optical indirect transitions of semiconducting $BaPb_{1-x}Bi_xO_3$. *Physical Review B, 55*, 15393.
16. Kunc, K., Zeyher, R., Liechtenstein, A. I., Methfessel, M., & Andersen, O. K. (1991). Ab-initio calculation of the charge and lattice modulation in $BaBiO_3$. *Solid State Communications, 80*, 325–329.
17. Franchini, C., Sanna, A., Marsman, M., & Kresse, G. (2010). Structural, vibrational, and quasiparticle properties of the Peierls semiconductor $BaBiO_3$: A hybrid functional and self-consistent GW+vertex-corrections study. *Physical Review B, 81*, 085213.
18. Shtarev, D. S., Shtareva, A. V., Mikhailovski, VJu., & Nashchochin, E. O. (2019). On the influence of strontium carbonate on improving the photocatalytic activity of strontium bismuthate $Sr_6Bi_2O_{11}$. *Catalysis Today, 335*, 492–501.
19. Shtarev, D. S., Shtareva, A. V., Kevorkyants, R., & Syuy, A. V. (2021). Synthesis, characterization, optoelectronic and photocatalytic properties of $Sr_2Bi_2O_5/SrCO_3$ and $Sr_3Bi_2O_6/SrCO_3$ heterostructures with varying $SrCO_3$ content. *Chemosphere, 267*, 129229. https://doi.org/10.1016/j.chemosphere.2020.129229
20. Shtarev, D. S., Shtareva, A. V., Ryabchuk, V. K., Rudakova, A. V., & Serpone, N. (2019). Considerations of trends in heterogeneous photocatalysis. Correlations between conduction and valence

band energies with bandgap energies of various photocatalysts. *ChemCatChem, 11*, 3534–3541.

21. Shtarev, D. S., Ryabchuk, V. K., Rudakova, A. V., Shtareva, A. V., Molokeev, M. S., Kirichenko, E. A., & Serpone, N. (2020). Phenomenological rule from correlations of conduction/valence band energies and bandgap energies in semiconductor photocatalysts: calcium bismuthates versus strontium bismuthates. *ChemCatChem, 12*, 1551–1555.
22. Bruker AXS TOPAS V4. (2008). *General profile and structure analysis software for powder diffraction data.—User's Manual*. Bruker AXS, Karlsruhe, Germany.
23. NIST X-ray Photoelectron Spectroscopy Database: see http://srdata.nist.gov/ and/or https://doi.org/10.18434/T4T88K
24. Shtarev, D. S., Shtareva, A. V., Ryabchuk, V. K., Rudakova, A. V., Murzin, P. D., Molokeev, M. S., Koroleva, A. V., Blokh, A. I., & Serpone, N. (2020). Solid-state synthesis, characterization, UV-induced coloration and photocatalytic activity—The $Sr_6Bi_2O_{11}$, $Sr_3Bi_2O_6$ and $Sr_2Bi_2O_5$ bismuthates. *Catalysis Today, 340*, 70–85.
25. Braslavsky, S. E., Braun, A. M., Cassano, A. E., Emeline, A. V., Litter, M. I., Palmisano, L., Parmon, V. N., & Serpone, N. (2011). Glossary of terms used in photocatalysis and radiation catalysis (IUPAC Recommendations 2011). *Pure & Applied Chemistry, 83*, 931–1014.
26. Shtarev, D. S., Shtareva, A. V., Blokh, A. I., Goncharova, P. S., & Makarevich, K. S. (2017). On the question of the optimal concentration of benzoquinone when it is used as a radical scavenger. *Applied Physics A, 123*, 602.
27. Goedecker, S., Teter, M., & Hutter, J. (1996). Separable dual-space Gaussian pseudopotentials. *Physical Review B, 54*, 1703–1710.
28. Perdew, J. P., Burke, K., & Ernzerhof, M. (1996). Generalized gradient approximation made simple. *Physical Review Letters, 77*, 3865–3868.
29. Perdew, J. P., Burke, K., & Ernzerhof, M. (1997). Generalized gradient approximation made simple (Erratum). *Physical Review Letters, 78*, 1396–1396.
30. Gonze, X., Amadon, B., Anglade, P. M., Beuken, J.-M., Bottin, F., Boulanger, P., Bruneval, F., Caliste, D., Caracas, R., Cote, M., Deutsch, T., Genovese, L., Ghosez, Ph., Giantomassi, M., Goedecker, S., Hamann, D., Hermet, P., Jollet, F., Jomard, G., … Zwanziger, J. W. (2009). ABINIT: first-principles approach to material and nanosystem properties. *Computer Physics Communications, 180*, 2582–2615.
31. Troullier, N., & Martins, J. L. (1991). Efficient pseudopotentials for plane-wave calculations. *Physical Review B, 43*, 1993–2006.
32. Hartwigsen, C., Goedecker, S., & Hutter, J. (1998). Relativistic separable dual-space Gaussian pseudopotentials from H to Rn. *Physical Review B, 58*, 3641–3662.
33. Monkhorst, H. J., & Pack, J. D. (1976). Special points for Brillouin-zone integrations. *Physical Reviw B, 13*, 5188–5192.
34. Williams, T., Kelley, C., Merritt, E.A., Bersch, C., Bröker, H.-B., Campbell, J., Cunningham, R., Denholm, D., Elber, G., Fearick, R., Grammes, C., Hart, L., Hecking, L., Juhász, P., Koenig, T., Kotz, D., Kubaitis, E., Lang, R., Lecomte, T., Lehmann, A., Lodewyck, J., Mai, A., Märkisch, B., Mikulík, P., Sebald, D., Steger, C., Takeno, S., Tkacik, T., van der Woude, J., van Zandt, J.R., Woo, A., & Zellner, J. (2018). *Gnuplot 5.2: An interactive plotting program*. see https://www.solvercube-com/gnuplot-a-command-line-driven-graphing-utility/ (accessed Mar 2021).
35. Efremov, V. A., Zakharov, N. D., Kuz'micheva, G. M., Mukhin, B. V., & Chernyshev, V. V. (1993). Yttrium-scandium-gallium garnet: the crystal structure. *Russian Journal of Inorganic Chemistry, 38*, 203–207.
36. Campbell, B. J., Stokes, H. T., Tanner, D. E., & Hatch, D. M. (2006). ISODISPLACE: A web-based tool for exploring structural distortions. *Journal of Applied Crystallography, 39*, 607–614.
37. "checkCIF", a service of the International Union of Crystallography: See https://checkcif.iucr.org/
38. FIZKarlsruhe, Leibnitz Institute for Information Infrastructure, Advancing Science: See http://www.fiz-karlsruhe.de/request_for_deposited_data.html
39. Castro, M. C., Jr., Carvalho, E. F. V., Paraguassu, W., Ayala, A. P., Snyder, F. C., Lufaso, M. W., & de Arahujo Paschoal, C. W. (2009). Temperature-dependent Raman spectra of Ba_2BiSbO_6 ceramics. *Journal of Raman Spectroscopy, 40*, 1205–1210.
40. de Waal, D., Range, K.-J., Konigstein, M., & Kiefer, W. (1998). Raman spectra of the barium oxide peroxide and strontium oxide peroxide series. *Journal of Raman Spectroscopy, 29*, 109–113.
41. Talha, M., & Lee, Y. W. (2020). Raman modes and dielectric relaxation properties of epitaxial $BaBiO_3$ thin films. *Materials Research Express, 7*, 016420.
42. Hardcastle, F. D., & Wachs, I. E. (1992). The molecular structure of bismuth oxide by Raman spectroscopy. *Journal of Solid State Chemistry, 97*, 319–331.
43. Poungchan, G., Ksapabutr, B., & Panapoy, M. (2016). One-step synthesis of flower-like carbon-doped ZrO_2 for visible-light-responsive photocatalyst. *Materials & Design, 89*, 137–145.
44. Shtarev, D. S., Shtareva, A. V., Kevorkyants, R., Rudakova, A. V., Molokeev, M. S., Bakiev, T. V., Bulanin, K. M., Ryabchuk, V. K., & Serpone, N. (2020). Materials synthesis, characterization and DFT calculations of the visible-light-active perovskite-like barium bismuthate $Ba_{1.264(4)}Bi_{1.971(4)}O_4$ photocatalyst. *Journal of Materials Chemistry C, 8*, 3509–3519.
45. Ji, X., Lu, J.-F., Wang, Q., & Zhang, D. (2020). Impurity doping approach on bandgap narrowing and improved photocatalysis of $Ca_2Bi_2O_5$. *Powder Technology, 376*, 708–723.
46. Chambers, S. A., Droubay, T., Kaspar, T. C., Gutowski, M., & van Schilfgaarde, M. (2004). Accurate valence band maximum determination for $SrTiO_3$ (001). *Surface Science, 554*, 81–89.
47. Fu, H., Pan, C., Yao, W., & Zhu, Y. (2005). Visible-light-induced degradation of rhodamine B by nanosized Bi_2WO_6. *Journal of Physical Chemistry B, 109*, 22432–22439.
48. Nelson, D. L., & Cox, M. M. (2012). *Lehninger principles of biochemistry* (6th ed.). New York: WH Freeman and Company.
49. Drake, H. L., Kusel, K., & Matthies, C. (2006). Acetogenic prokaryotes. *The Prokaryotes, 2*, 354–420.
50. Pavitt, A. S., Bylaska, E., & Tratnyek, P. G. (2017). Oxidation potentials of phenols and anilines: correlation analysis of electrochemical and theoretical values. *Environmental Science: Processes & Impacts, 19*, 339–349. https://doi.org/10.1039/C6EM00694A

Authors and Affiliations

Dmitry S. Shtarev[1] · Anna V. Shtareva[1] · Ruslan Kevorkyants[2] · Maxim S. Molokeev[3,4,5] · Nick Serpone[6]

✉ Nick Serpone
nick.serpone@unipv.it; nickserpone@yahoo.ca

Dmitry S. Shtarev
shtarev@mail.ru

Anna V. Shtareva
avshtareva@mail.ru

Ruslan Kevorkyants
ruslan.kevorkyants@gmail.com

Maxim S. Molokeev
msmolokeev@mail.ru; thehgat@gmail.com

[1] Laboratory of Thin Film Technologies, Far Eastern Federal University, Ajax Bay 10, Russky Island, Vladivostok 690922, Russia

[2] Laboratory 'Photoactive Nanocomposite Materials', St. Petersburg State University, Ulyanovskaya 1, St. Petersburg 198504, Russia

[3] Far Eastern State Transport University, Serysheva 47, Khabarovsk 680021, Russia

[4] Kirensky Institute of Physics, Akademgorodok 50, bld. 38, Krasnoyarsk 660036, Russia

[5] Siberian Federal University, Svobodny 79, Krasnoyarsk 660041, Russia

[6] PhotoGreen Laboratory, Dipartimento di Chimica, Università di Pavia, via Taramelli 12, Pavia 27100, Italy